Molecular Catalysis 446 (2018) 58–71

Contents lists available at ScienceDirect

Molecular Catalysis

journal homepage: www.elsevier.com/locate/mcat

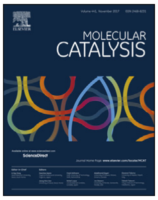

$Cs_xH_{3-x}PW_{12}O_{40}$ nanoparticles dispersed in the porous network of Zr-pillared α-zirconium phosphate as efficient heterogeneous catalyst for synthesis of spirooxindoles

Sagnika Pradhan, B.G. Mishra*

Department of Chemistry, National Institute of Technology, Rourkela 769008, Odisha, India

ARTICLE INFO

Article history:
Received 19 June 2017
Received in revised form 8 December 2017
Accepted 12 December 2017

Keywords:
Phosphotungstic acid
α-ZrP
Spirooxindole
UV–vis-DRS
HRTEM

ABSTRACT

Layered α-zirconium phosphate (α-ZrP) was prepared by reflux method using $ZrOCl_2.8H_2O$ and H_3PO_4 as precursor. The α-ZrP material was pillared with Zr-oxyhydroxy nanoclusters to prepare Zr-pillared α-zirconium phosphate (ZZP). An enhancement in interlayer spacing, surface area and porosity was noticed as a result of Zr-pillaring. The cesium exchanged phosphotungstic acid ($Cs_xH_{3-x}PW_{12}O_{40}$) nanoparticles were dispersed in the porous matrix of ZZP material to prepare $Cs_xH_{3-x}PW_{12}O_{40}$-ZZP nanocomposite systems. The nanocomposites were characterized using XRD, FTIR, UV–vis-DRS, TGA-DTA, XPS, N_2 sorption, TPD, FESEM and HRTEM techniques. The expansion in layer structure of α-ZrP upon pillaring and its subsequent retention in the composite material was noticed from XRD. UV–vis and FTIR study indicated structural integrity of the $Cs_xH_{3-x}PW_{12}O_{40}$ nanoclusters in the ZZP interlayer. The surface area of the composite materials was in the range of 80–130 $m^2 g^{-1}$. The composite materials contained significantly higher amount of medium and strong acidic sites compared to the ZP and ZZP materials. Microscopic study suggested the presence of hierarchical nanospheres with diameter between 150 and 200 nm. The presence of well dispersed $Cs_xH_{3-x}PW_{12}O_{40}$ nanoparticles with size between 8 and 15 nm was confirmed from HRTEM study. The nanocomposite materials were used as efficient heterogeneous catalyst for synthesis of spirooxindoles by multicomponent one pot condensation of isatin, malononitrile, naphthol/1,3-diketones. Structurally diverse spirooxindole derivatives were synthesized in high yield and purity in short span of time using the $Cs_xH_{3-x}PW_{12}O_{40}$-ZZP nanocomposites as catalyst under mild conditions.

1. Introduction

Zirconium phosphates (ZrP) are a class of versatile materials used in many advanced applications such as proton conducting membrane, ion exchanger, solid state gas sensor, adsorbent and as substrate for immobilization of biological materials [1–3]. These materials possess surface acidic functionality which are water tolerant, thermally stable and hence are suitable for application in acid catalyzed organic transformations [4]. Among different structural forms of zirconium phosphates, α-zirconium phosphate is the most widely investigated material in catalysis [1,2]. In recent years, efforts have been devoted to prepare engineered catalytic materials by modification of the interlayer space and layer composition of the ZrP material. Several organomodified ZrP materials have been reported in literature and studied for selective drug delivery and catalysis [1,3]. The other important characteristics of ZrP material are the exfoliation of the layers in polar solvents and presence of exchangeable interlayer protons. These properties have been exploited to ion exchange the protons with surfactant molecules, inorganic cationic nanoclusters as well as bulky organic moieties to form expanded structures with porosity and high surface area [2,5–10]. The pillared α-ZrP materials prepared by intercalation of inorganic cationic clusters of Al, Ti, Cr, Fe-Cr, Zr and Si into the interlayer space are a class of promising materials for catalysis [8–17]. The intercalation of these inorganic nanoclusters imparts structural rigidity and significantly improves the surface area and pore volume of α-ZrP. The pillared materials also exhibit enhanced surface acidity which is reflected in their higher catalytic activity

---

* Corresponding author.
E-mail addresses: brajam@nitrkl.ac.in, bgmcat@rediffmail.com (B.G. Mishra).

https://doi.org/10.1016/j.mcat.2017.12.013
2468-8231/

for acid catalyzed reactions [8–15]. In addition to their application as heterogeneous acid catalyst, the pillared α-ZrP materials due to their high surface area and uniform porosity have been used as support for catalytically active phases. For example, the alumina pillared α-ZrP material has been used an efficient support for the Ni-Mo hydrodesulfurization catalyst [16] and Cu catalyst for reduction of NO with propane [17]. Although there are reports on the catalytic application of the pillared α-ZrP material, there is no study dealing with the catalytic application of these materials for synthesis of biologically important molecules. In this work, we have used the porous matrix of Zr-pillared α-ZrP material as carrier for catalytically active $Cs_xH_{3-x}PW_{12}O_{40}$ nanoparticles and studied their catalytic application for synthesis of biologically important spirooxindoles.

The metal insoluble salts of heteropoly acids (HPAs) obtained by partially exchanging the labile protons of HPA with large monovalent ions such as Cs^+, NH_4^+, K^+, Ag^+ are attractive materials for application in heterogeneous catalysis [18–23]. These materials possess improved physicochemical characteristics such as high surface area, evolved porosity and enhanced acidity compared to the parent HPA. In recent years, the Cs^+ exchanged phosphotungstic acid ($Cs_xH_{3-x}PW_{12}O_{40}$) has been studied widely as a promising heterogeneous catalyst for acid catalyzed reactions. The $Cs_xH_{3-x}PW_{12}O_{40}$ material exhibits superior catalytic activity for Beckmann rearrangement, alkylation/acylation reactions, hydration of olefins, hydrocracking of extra-heavy oil, transesterification reactions, esterification of fatty acids and biodiesel synthesis [19–24]. These materials are known to exhibit composition dependent surface properties. Particularly, the $Cs_xH_{3-x}PW_{12}O_{40}$ material with x = 2.0–2.5, display higher catalytic activity than the parent $H_3PW_{12}O_{40}$ [20,21]. The catalytic utility of $Cs_xH_{3-x}PW_{12}O_{40}$ materials has been further enhanced by dispersing them on high surface area support [24–27]. The $Cs_xH_{3-x}PW_{12}O_{40}$ material dispersed over catalytically active functional supports such as ZrO_2, SnO_2 have been studied recently for unsymmetrical ether synthesis and carbonolysis and etherification of glycerol [25–27]. A synergistic effect between the acidic sites of the support and the active phase has been invoked to explain the higher catalytic activity of the supported system.

Indole has been widely discovered as a pharmacophore, which represents many natural isolates of diverse biological activity [28]. In the past, several natural products containing indole nucleus particularly 3-substituted indoles and spirooxindoles have been isolated [28,29]. The heterocyclic spirooxindole ring is found in a number of pharmaceutical compounds including horsfiline, alstonisine, coerulescine, spirotryprostatins A and elacomine [30]. It has also been observed that spirooxindole compounds containing substituted fused 4H-chromenes display a wide range of useful biological properties, including spasmolitic, diuretic, anticoagulant, anticancer, and antianaphylactic activities [31–33]. In view of the therapeutic properties and biological relevance, the synthesis of these compounds has received considerable attention from synthetic chemists. The most effective route for synthesis of spirochromene derivatives involves the catalytic multicomponent condensation of isatin, active methylene compound, and 1,3-dicarbonyl compounds [34]. Several catalytic protocols have been developed in the recent past for the synthesis of these biologically important compounds which include the use of $InCl_3$, sodium stearate, sulfamic acid, triethylbenzylammonium chloride (TEBA), Fe_3O_4@SiO_2-imid-PMA, amino-functionalized SBA-15, ZnS nanoparticles, nano MgO and guanidine functionalized magnetic Fe_3O_4 nanoparticles as catalyst [33–40]. However, many protocols use homogeneous catalysts at elevated temperatures giving moderate to good yield of the product. Although the investigated heterogeneous catalytic protocols offer advantages in term of reusability of the catalyst, some protocols involve complex catalytic system requiring multiple steps and costly chemicals for their synthesis. Keeping in mind the merits and demerits of the developed methods; we feel that there is scope to develop novel heterogeneous catalytic protocol for synthesis of spirooxindole under mild conditions. In this work, we have used $Cs_xH_{3-x}PW_{12}O_{40}$ nanoparticles dispersed in the porous matrix of Zr-pillared α-ZrP material as efficient catalyst for synthesis of structurally diverse spirooxindole derivatives.

2. Materials and methods

Zirconyl chloride ($ZrOCl_2{\cdot}8H_2O$), phosphoric acid (H_3PO_4), phosphotungstic acid ($H_3PW_{12}O_{40}$) and cesium carbonate (Cs_2CO_3) were procured from Hi media Chemicals Pvt. Ltd., India. All chemicals used in this study were of AR grade (>99.9% purity) which was used directly in the experiments without further purification. Deionized water prepared in the laboratory was used for material synthesis.

2.1. Preparation of α-zirconium phosphate (ZP)

The α-zirconium phosphate material was prepared using the procedure described in the literature [7,8]. Briefly, 10 g of $ZrOCl_2{\cdot}8H_2O$ was added to 100 ml of 12 M H_3PO_4 solution and refluxed at 100 °C for 24 h. The obtained white precipitate was filtered, washed repeatedly with hot water to remove Cl^- ions and centrifuged at 5000 rpm. The solid material was subsequently dried in a hot air oven at 90 °C for 24 h to obtain the ZP material.

2.2. Preparation of Zr-pillared α-zirconium phosphate (ZZP)

2.2.1. Preparation of Zr-pillaring solution

A 0.1 M $ZrOCl_2{\cdot}8H_2O$ solution was prepared by dissolving the required amount of the salt in deionized water. The solution was subsequently refluxed for 24 h to prepare the pillaring solution.

2.2.2. Pillaring process

2 g of ZP was dispersed in 200 ml of 0.1 M *n*-butylamine solution and stirred for 24 h to prepare a well dispersed exfoliated colloidal suspension. Required amount of Zr-pillaring solution (ZP:$ZrOCl_2{\cdot}8H_20$ molar ratio 1:30) was then added dropwise (50 ml h^{-1}) to the colloidal suspension and refluxed at 100 °C for 24 h under constant stirring. After completion of the intercalation process, the solid material was recovered by centrifugation at 5000 rpm and washed repeated with hot water to remove the amine and chloride ions. The solid material was subsequently dried in a hot air oven at 80 °C for 12 h and calcined at 350 °C for 2 h to obtain the ZZP catalyst.

2.3. Preparation of $Cs_xH_{3-x}PW_{12}O_{40}$ dispersed over Zr-pillared α-zirconium phosphate (CPxZZP)

The 20 wt% $Cs_xH_{3-x}PW_{12}O_{40}$ supported over ZZP material was prepared by ion exchange of H^+ with Cs^+ ions followed by wet impregnation. In a typical procedure, 2 g of ZZP material was dispersed in 20 ml water by sonication for 20 min. To this aqueous dispersion, 0.4 g of $H_3PW_{12}O_{40}$ was added and stirred for 2 h. Stoichiometric amount of 0.5 mmol Cs_2CO_3 solution was then added dropwise to this suspension and stirred for 6 h at room temperature. The temperature was then raised to 90 °C and was heated continuously under stirring to remove the excess water. The resulting material was dried in air at 120 °C for 6 h followed by calcination at 350 °C for 2 h to obtain the $Cs_xH_{3-x}PW_{12}O_{40}$/ZZP material. Using this procedure 20 wt% $Cs_1H_2PW_{12}O_{40}$ and $Cs_2H_1PW_{12}O_{40}$ supported over ZZP material were prepared. These supported materials are referred to as CPxZZP in the subsequent text, where x represent the number of moles of Cs^+ ions replacing the H^+ ions from $H_3PW_{12}O_{40}$.

2.4. Characterization techniques

The powder XRD patterns of the CPxZZP materials were recorded with a Rigaku Ultima IV multipurpose X-ray diffraction system using CuKα (λ = 1.5418 Å) radiation in the 2θ range of 2–50° with a scan speed of $2^\circ\,min^{-1}$. The specific surface areas were determined by BET method using N_2 adsorption/desorption at 77 K on a Quantachrome autosorb gas sorption system. The composite samples were degassed at 150 °C for 6 h prior to the sorptometric studies. Thermogravimetric analysis was performed using a Perkin-Elmer TGA-7 apparatus in air atmosphere ($30\,ml\,min^{-1}$) with a linear heating rate ($10\,^\circ C\,min^{-1}$) from room temperature to 700 °C. Microscopic analysis was carried out using FESEM (Nova Nano SEM/FEI microscope) and HRTEM (TECNAI 300kV) techniques. The UV–vis-DR spectra of the composite materials were recorded using a Jasco V-650 spectrometer. The FTIR spectra were obtained in transmittance mode using a Perkin-Elmer infrared spectrometer with a resolution of $4\,cm^{-1}$, in the range of $400–4000\,cm^{-1}$. The X-ray photoelectron spectra of CP_2ZZP sample was recorded using SPECS make (Germany) spectrophotometer with 150 mm hemispherical analyzer at band pass energy of 12 eV. Monochromatic AlKα radiation of 1486.74 eV was used as X-ray source. Binding energy corrections due to electrostatic charging was made relative to the C1s peak at 284.6 eV. The number of acidic sites was estimated by ammonia TPD experiments using a Micromeritics AutoChem II 2920 chemisorption apparatus equipped with a TCD detector. Prior to NH_3 adsorption, approximately 250 mg of sample was treated at 350 °C for 2 h under flowing He and then cooled to room temperature under He environment. Subsequently, the sample was exposed to flowing ammonia gas mixture (5% NH_3 in He) for 1 h, and then purged by He gas for 30 min to remove excess physisorbed ammonia. The NH_3-TPD profiles were recorded from room temperature to 700 °C at a rate of $10\,^\circ C\,min^{-1}$. The ^1H NMR spectra were recorded with Bruker 400 MHz NMR spectrometer using TMS as internal standard.

2.5. Catalytic study for synthesis of spirooxindoles

The synthesis of spirooxindole was carried out by one pot condensation of isatin, naphthol/1,3-diketones and malononitrile using CPxZZP catalyst. In a typical procedure, 1 mmol each of isatin, α- naphthol and malononitrile was dissolved in 5 ml of acetonitrile to which 50 mg of CP_2ZZP catalyst was added. The reaction mixture was stirred for 1.5 h at 60 °C. The progress of the reaction was monitored using TLC. After completion of the reaction, the catalyst particles were filtered from the reaction mixture and the crude product was recovered. The crude product was further recrystallized from hot ethanoic solution to get the pure product.

3. Results and discussion

3.1. Characterization of $Cs_xH_{3-x}PW_{12}O_{40}$ dispersed over Zr-pillared α-zirconium phosphate (CPxZZP) materials

The XRD patterns of the CPxZZP materials together with the ZP, ZZP, $H_3PW_{12}O_{40}$ and $Cs_2H_1PW_{12}O_{40}$ (Cs_2PWA) are presented in Figs. 1 and 2. In the 2θ range of 2–10°, the ZP material does not show any well-defined XRD peak. The peak at 2θ value of 11.8° corresponds to reflection from the (002) planes with an interlayer spacing of 7.5 Å (Fig. 1a). This value is in agreement with earlier literature reports and indicates alignment of the α-ZrP sheets along the axial direction [1,2]. Upon pillaring with the Zr-polycations, considerable expansion of the interlayer structure is observed. The ZZP material exhibits a broad XRD peak with d spacing value of 34.0 Å (Fig. 1b). The intercalation of the Zr-oligomeric clusters into the α-ZrP interlayer has moved apart the ZrP sheets resulting in an enhanced interlayer space. The low angle XRD feature has been found to be preserved in the CPxZZP material indicating the retention of the layer structure (Fig. 1c &d). The CPxZZP materials exhibit basal spacing in the range of 27.5–29.0 Å. Assuming the layer thickness of α-ZrP sheets to be 6.5 Å [1], these materials exhibit interlayer gallery height between 21.0 and 22.5 Å. The observed result suggests a clear enhancement in the interlayer free space as a

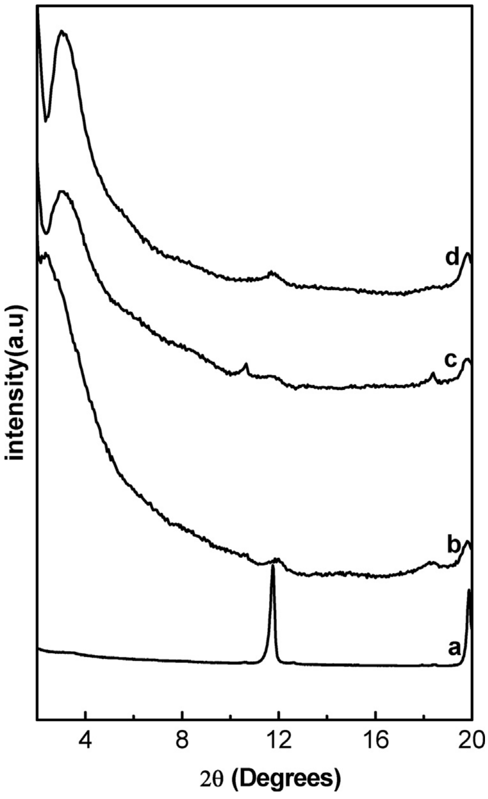

Fig. 1. Low angle XRD patterns of (a) ZP, (b) ZZP, (c) CP_1ZZP and (d) CP_2ZZP materials.

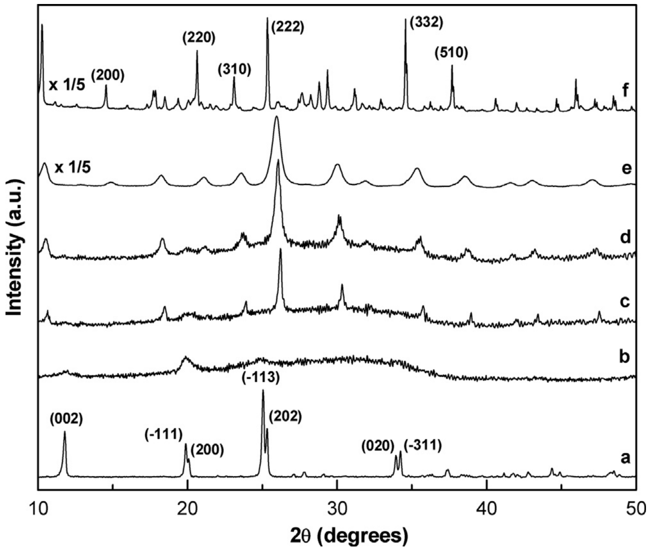

Fig. 2. XRD patterns of (a) ZP, (b) ZZP, (c) CP_1ZZP, (d) CP_2ZZP, (e) Cs_2PWA and (f) PWA materials.

Table 1
Physicochemical characteristics of CPxZZP materials.

Material	Specific surface area ($m^2 g^{-1}$)	Pore volume ($cm^3 g^{-1}$)	Crystallite size of Cs_xPWA (nm)	NH_3 desorption ($mmol g^{-1}$)			Total acidity ($mmol g^{-1}$)
				<250 °C	250–450 °C	>450 °C	
ZP	46.8	0.09	–	0.12	0.07	0.04	0.23
ZZP	133.9	0.19	–	0.10	0.14	0.08	0.32
CP_1ZZP	96.4	0.11	18.1	0.06	0.20	0.15	0.41
CP_2ZZP	107.7	0.14	9.2	0.08	0.24	0.16	0.48

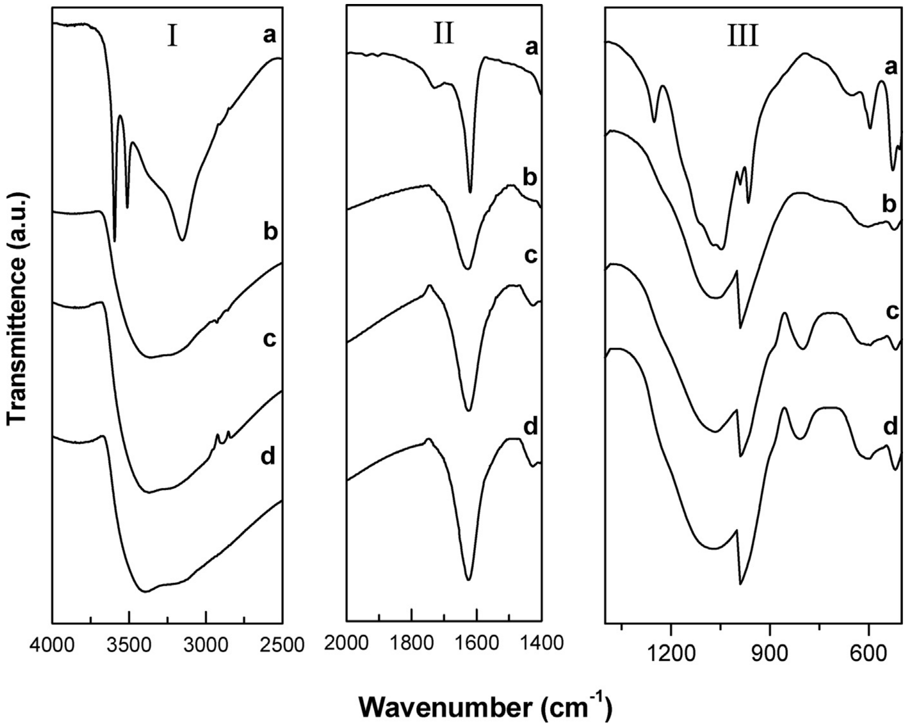

Fig. 3. FTIR spectra of (a) ZP, (b) ZZP, (c) CP_1ZZP, and (d) CP_2ZZP materials.

result of intercalation of Zr-oligomeric clusters. Zr^{4+}ions are known to form stable tetrameric clusters $[Zr_4(OH)_8(H_2O)_{16}]^{8+}$ with size 8.9 × 8.9 × 5.8 Å^3 in dilute acidic solutions. At elevated temperature, further hydrolysis and condensation of these tetrameric clusters into larger clusters have been reported [41]. In the present study, the increase in the basal spacing can be ascribed to the intercalation of larger Zr-oligomeric clusters into the α-ZrP interlayer. In the 2θ range of 20–50°, the α-ZrP material displays a series of discrete and well defined XRD peaks with d spacing values of 7.5, 4.46, 4.41, 3.54, 3.51, 2.63 and 2.61 Å (Fig. 2a). These peaks correspond to the reflections from the (002), (−111), (200), (−113), (202), (020) and (−311) planes of monoclinic $Zr(HPO_4)_2(H_2O)$ (space group- P21/n, JCPDS-ISDD No.-70-0561). The ZZP and CPxZZP materials display broad and less intense peaks in comparison to the α-ZrP phase (Fig. 2b–d). This observation indicates a partial loss of crystallinity due to pillaring and subsequent dispersion of Cs_xPWA particles. During the pillaring process, complete exfoliation of α-ZrP sheets takes place due to intercalation of *n*-butyl amine as a layer expansion agent. When the sheets are reassembled in presence of the Zr-oligomeric clusters the stacking of the α-ZrP sheets is favored along the z-direction. However, the long range ordering along other crystallographic directions is affected due to the inclusion of the Zr-oligomeric clusters. Commercially procured $H_3PW_{12}O_{40}{\cdot}xH_2O$ (PWA) shows highly intense and narrow XRD peaks with d spacing value of 8.4, 4.86, 3.41, 2.96, 2.53, 2.32 Å corresponding to the secondary cubic crystalline structure (space group-Pn3m, JCPDS ISDD No-75-2125) (Fig. 2f). The XRD profile of $Cs_2H_1PW_{12}O_{40}$ (Cs_2PWA) material is presented in Fig. 2e. No peaks corresponding to the free acid could be detected for the Cs_2PWA sample. The peaks are usually broad and shifted to higher 2θ values in comparison to the $H_3PW_{12}O_{40}$. Similar XRD features are also noted for CP_1ZZP and CP_2ZZP materials (Fig. 2c & d). The shift in the peak position, in comparison to the parent $H_3PW_{12}O_{40}$ phase, can be assigned to the formation of a distinct body-centered cubic structure of $Cs_3PW_{12}O_{40}$ salt consistent with earlier observation [19,42]. It has been reported that the Cs exchanged $H_3PW_{12}O_{40}$ with different degree of substitutions contain a core of ultrafine crystallites of $Cs_3PW_{12}O_{40}$ salt over which the free acids are deposited epitaxially [19,42]. In the present study, the similarity in the XRD features of CP_1ZZP and CP_2ZZP materials with Cs_2PWA phase indicates that the CPxZZP materials contain $Cs_3PW_{12}O_{40}$ salt as a distinct phase. The average crystallite size of the supported CsxPWA phase is calculated from the Fourier line profile analysis of the broadened XRD profiles using Warren-Averbach method using Bredth software [43]. The volume average crystallite size distribution of the supported CsxPWA phase along with pure Cs_2PWA is presented in Fig. S1. The crystallite size distribution is quite broad for CP_1ZZP materials whereas comparable narrow distribution is observed for Cs_2PWA and CP_2ZZP materials. The average crystallite sizes calculated from the initial slope of As ∼ L plot (Fig. S2) are presented in Table 1. The

Cs_2PWA material contains crystallite with average size of 4.8 nm. With increase in Cs content in the supported material the crystallite size of the CsxPWA phase is found to decrease.

The FTIR spectra of ZP, ZZP and CPxZZP materials are presented in Fig. 3. In the stretching frequency region, the ZP material exhibits discrete peaks at 3591 and 3512 cm^{-1}, corresponding to the PO—H stretching vibration of structural hydroxyl groups (Fig. 3I a). The peak at 3150 cm^{-1} can be assigned to O—H stretching of interlayer water molecules [7]. After pillaring with the Zr-polycations and subsequent dispersion of Cs_xPWA species, broad and intense IR bands are observed in this spectral region (Fig. 3I b–d). The broadness of the stretching bands is due to the presence of different types of O—H species originating from the α-ZrP layers, Zr-pillars and the dispersed Cs_xPWA species interacting with each other through hydrogen bonding. In the spectral region of 1500–2000 cm^{-1}, all materials exhibit a strong IR band at 1625–1630 cm^{-1}, the intensity of which increases upon pillaring and modification with Cs_xPWA species (Fig. 3II). This band has been assigned to the O—H bending vibration of structural water as well as water molecules present in the primary coordination sphere of the Zr-nanopillars [41]. In the finger print region of 400–1400 cm^{-1}, the α-ZrP material shows a series of discrete IR bands at 1251, 1050, 962 and 595 cm^{-1} (Fig. 3III a). The peaks at 1251 and 595 cm^{-1} can be assigned to the P—OH stretching and in plane deformation vibrations whereas the 1050 and 962 cm^{-1} peaks are characteristic vibrations of phosphate groups [7,14,15]. In this spectral region, the ZZP material retains all the vibrations of α-ZrP (Fig. 3III b). After dispersion of the Cs_xPWA species, new IR bands are observed at 1070, 885 and 800 cm^{-1} corresponding to the ν_{as}(P—O), ν(W—O_c—W) and ν(W—O_e—W) vibrations from the Keggin heteropoly structure (Fig. 3III c & d) [19,20,25]. The FTIR study confirms the structural integrity of the Cs_xPWA and α-ZrP species in the composite materials.

The UV–vis-DR spectra of CPxZZP materials along with the pure components are presented in Fig. 4. Pure α-ZrP material exhibits a low intense UV band with maxima at 233 nm due to the O → P charge transfer transition (Fig. 4I a). Upon pillaring with Zr-oxyhydroxy clusters a strong UV absorption feature is noticed at 208 nm along with a broad shoulder at 290 nm (Fig. 4I b). The 208 nm peak can be assigned to $O^{2-} \rightarrow Zr^{4+}$ charge transfer transition of the zirconia pillars present in the α-ZrP interlayer [41]. Zirconia is a direct band gap insulator which shows an interband transition in the UV region of the spectrum. Among the polymorphic form of ZrO_2, the octacoordinated tetragonal phase shows absorption maxima in the range of 205–215 nm whereas the heptacoordinated monoclinic phase shows maxima at 245 nm [44,45]. With decrease in the number of coordinating O^{2-} ions from 8 to 6 the absorption maxima progressively shifts towards the lower energy side. Thus the peak at 208 nm can be assigned to the presence of octacoordinated t-ZrO_2 nanoclusters as pillars [41]. The 290 nm peak arises due to presence of defect centers in the t-ZrO_2 nanocrystallites. Such features have been observed earlier for ZrO_2 nanocrystallites which have been ascribed to the presence of localized state between valence and conduction bands [45]. The UV–vis spectra of pure $H_3PW_{12}O_{40}$ show three absorption maxima with absorption edge near 400 nm (Fig. 4II b). The absorption maxima at 215, 260 and 310 nm can be assigned to the $P^{5+} \longleftarrow O^{2-}$ and $W^{6+} \longleftarrow O^{2-}$ charge transfer from the edge and corner shared WO_6 octahedra of $H_3PW_{12}O_{40}$ [46]. The essential absorption features of the phosphotungstic acid are retained in the Cs_2PWA material (Fig. 4II a). The individual absorption peaks have broadened probably due to the structural rearrangement due to Cs^+ ion exchange. The CPxZZP material on the other hand exhibit distinct absorption features (Fig. 4I c & d). The absorption edge has shifted towards the higher energy side (commence near 350 nm) along with a significant reduction in intensity of the $W^{6+} \longleftarrow O^{2-}$ charge transfer transition. The decrease in the intensity of the $W^{6+} \longleftarrow O^{2-}$ charge transfer transition can be ascribed to strong interaction between the ZZP support and the Cs_xPWA clusters through W—O bond resulting in grafting of these species in the intra-particle pores as well as the open surfaces of the α-ZrP sheets. The shift in the band edge to lower wavelength can be ascribed to quantum confinement effect due to small crystallite size of the CsxPWA particles. It has been observed earlier that the Cs exchanged heteropoly acids contains small crystallites; display enhanced surface area and posrity [19–24]. This observation is further corroborated by TEM and Fourier analysis data where the crystallite size of the CsxPWA is observed in the range of 8–15 nm.

The thermal transformation behavior of the CP_2ZZP material along with pure ZP and ZZP materials is studied using combined TG-DTA technique (Fig. 5). The α-ZrP material shows 13% weight loss in the temperature range of 100–250 °C. In this temperature range, two endothermic peaks are observed in the DTA profile corresponding to the removal of the physisorbed interlayer water molecules as well as the coordinated water molecules (Fig. 5I) [14]. The water molecules in the coordination sphere of the phosphate ions are more strongly bonded and hence desorbs at higher temperature. Beyond 250 °C, the weight loss is more gradual up to 470 °C. The weight loss of 6.5% observed in the temperature range of 470–600 °C can be assigned to the degradation of the layer structure of α-ZrP leading to formation of pyrophosphates (Fig. 5I). Such thermal transformation behavior has been noted earlier for the α-ZrP material [6]. The ZZP and CP_2ZZP material exhibits similar low temperature weight loss feature with the exception that the weight loss is more pronounced for ZZP material (35 wt%) (Fig. 5II). This observation indicates a significant improvement in water retention capacity of the α-ZrP matrix as a result of pillaring. The pillaring process increases the interlayer spacing and porosity of the α-ZrP which is responsible for the improved water retention capacity. In the high temperature region, the ZZP material exhibits an exothermic peak at 320 °C due to the combustion of the residual intercalated *n*-butyl amine (Fig. 5II). Beyond 400 °C, the gradual weight loss feature corresponds to the thermal transformation of the pillars [14,15]. In addition to the low temperature weight loss feature, the CP_2ZZP material exhibits a second weight loss of 3 wt% between 500 and 600 °C. This weight loss corresponds to the decomposition of the primary structure of the Keggin ions (Fig. 5III) [24]. The TGA-DTA study indicates that the CP_2ZZP material is stable up to 500 °C.

The oxidation state of the elements and their chemical environment was probed using XPS study. The XPS spectra of CP_2ZZP material is presented in Fig. 6. The survey spectrum displays the characteristic features of Zr, P, W, Cs, O and S present in the composite sample (Fig. 6a). In the high resolution Zr 3d spectrum, two peaks are observed at 182.2 eV and 184.4 eV (Fig. 6b). These peaks correspond to the photoelectron emission from $3d_{3/2}$ and $3d_{5/2}$ energy states of tetravalent Zr(IV) species [47]. In the W4f region, a doublet is observed at 35.8 and 37.9 eV corresponding to the $4f_{7/2}$ and $4f_{5/2}$ energy states of W^{6+} species of the Keggin ions (Fig. 6c) [23]. The O1s spectrum is centered at 531.8 eV and is quite broad and asymmetric (Fig. 6d). The peak can be deconvoluted into three spectral regions with maxima at 531.2, 532.1 and 533.2 eV. The peak at 531.2 eV arises due to the combined contribution from W—O—W and the ZrO_2 pillars. ZrO_2 is known to exhibit O1s peak at 530.2–530.7 eV [48]. Hence, it is likely that the O from the ZrO_2 can contribute to this peak. The Keggin ions are known to exhibit an O1s peak at 532.6 eV due to photoemission from W—O—P and terminal oxygen (W=O) of the Keggin ion structure [49]. This peak appeared at 532.1 eV in the present study. This is probably due to the strong interaction of the terminal oxygens with the Zr^{4+} ions of the α-ZrP sheets. Zr^{4+} being more electropositive can increase the electron density around the terminal oxygen lowering their binding energy. This is further corroborated from UV study where a significant decrease

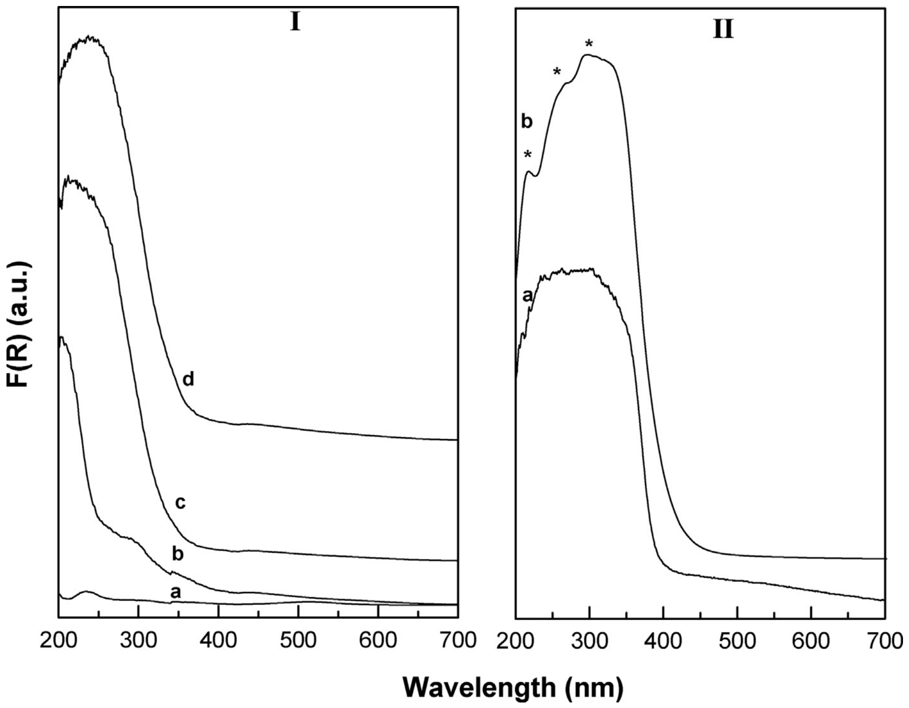

Fig. 4. UV–vis-DRS spectra of (a) ZP, (b) ZZP, (c) CP_1ZZP, and (d) CP_2ZZP (panel I) and (a) Cs_2PWA and (b) $H_3PW_{12}O_{40}$ (panel II).

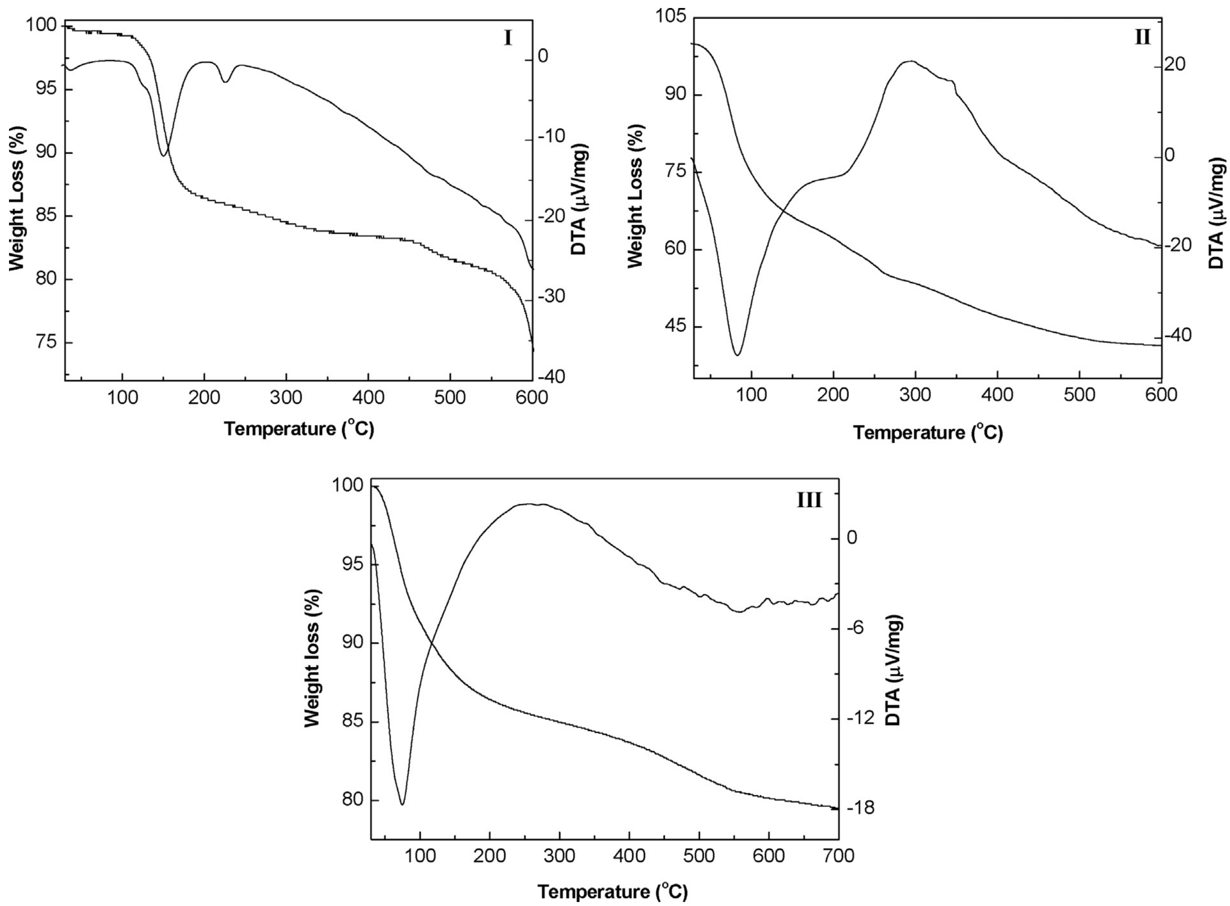

Fig. 5. TG-DTA profiles of (I) ZP, (II) ZZP and (III) CP_2ZZP materials.

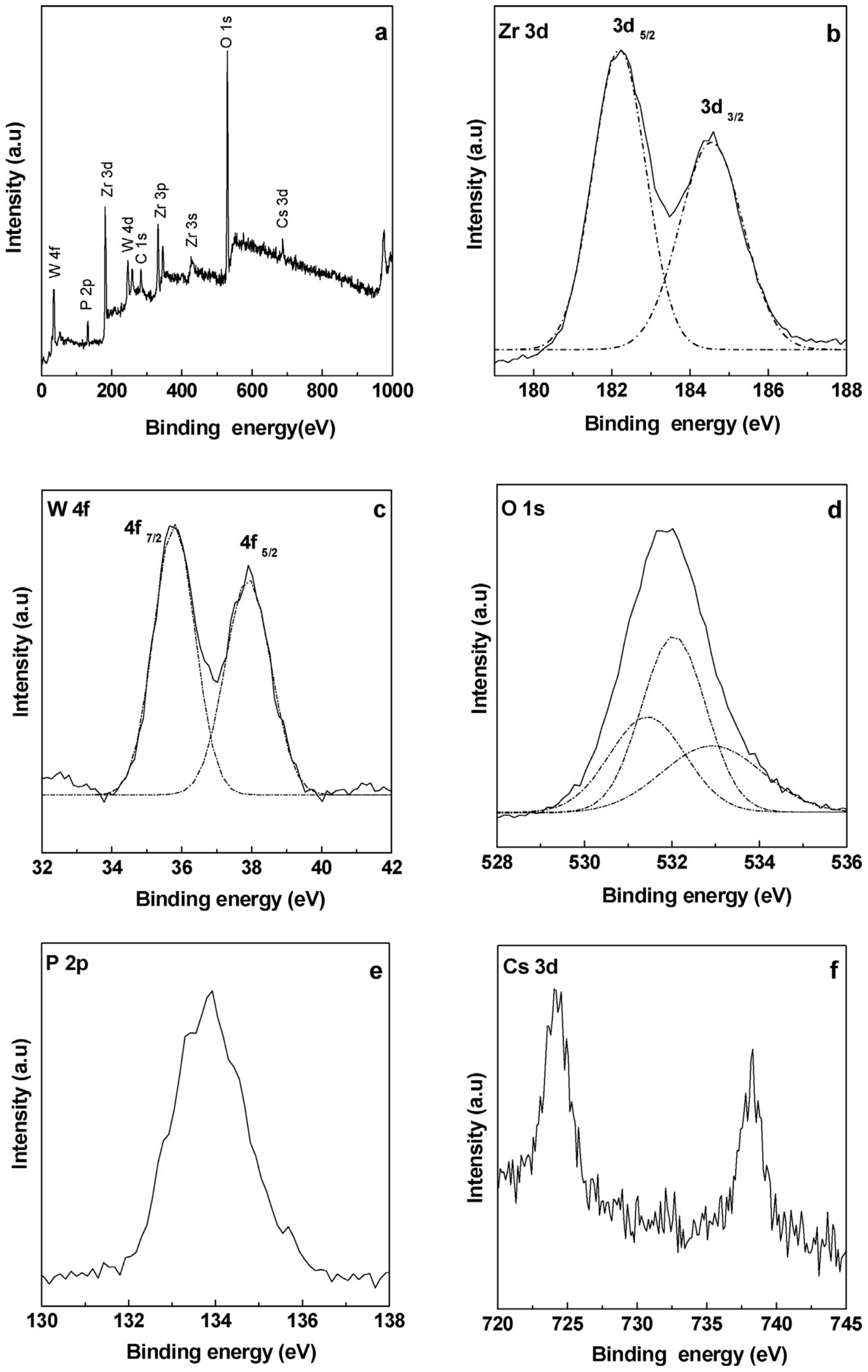

Fig. 6. XPS spectra of CP_2ZZP material.

in $W^{6+} \longleftarrow O^{2-}$ charge transfer transition has been observed for the supported species. The third O1s peak at 533.2 eV can be assigned to the phosphate ions of the α-ZrP sheets in line with the literature observation [47,50]. In the P2p region, a broad peak centered at 133.8 eV is characteristics of pentavalent tetracoordinated phosphorous (P^{5+}) (Fig. 6e). This peak arises due to the phosphate ions of the α-ZrP sheets and PO_4 species of the Keggin ions [47]. The occurrence of Cs^+ ions in CP_2ZZP material is confirmed from the spectral doublet at 724.2 and 738.2 eV corresponding to the photoemission from the $3d_{5/2}$ and $3d_{3/2}$ energy states of Cs^+ ions (Fig. 6f) [19].

The surface area and pore volume of the CPxZZP materials is evaluated using N_2 sorption at 77 K. The N_2 sorption isotherms of the CPxZZP material together with ZP and ZZP materials are presented in Fig. 7. The sorption isotherm for ZP material exhibits behavior between those of type-II and IV isotherm according to the BDDT classification (Fig. 7a) [12–15]. The amount of N_2 adsorption at low pressure range is quite less indicating very little porosity in micropore range. The observed hysteresis is H3 type according to the IUPAC classification indicating the presence of slit shaped pores or pores with space between parallel plates [51]. The pore

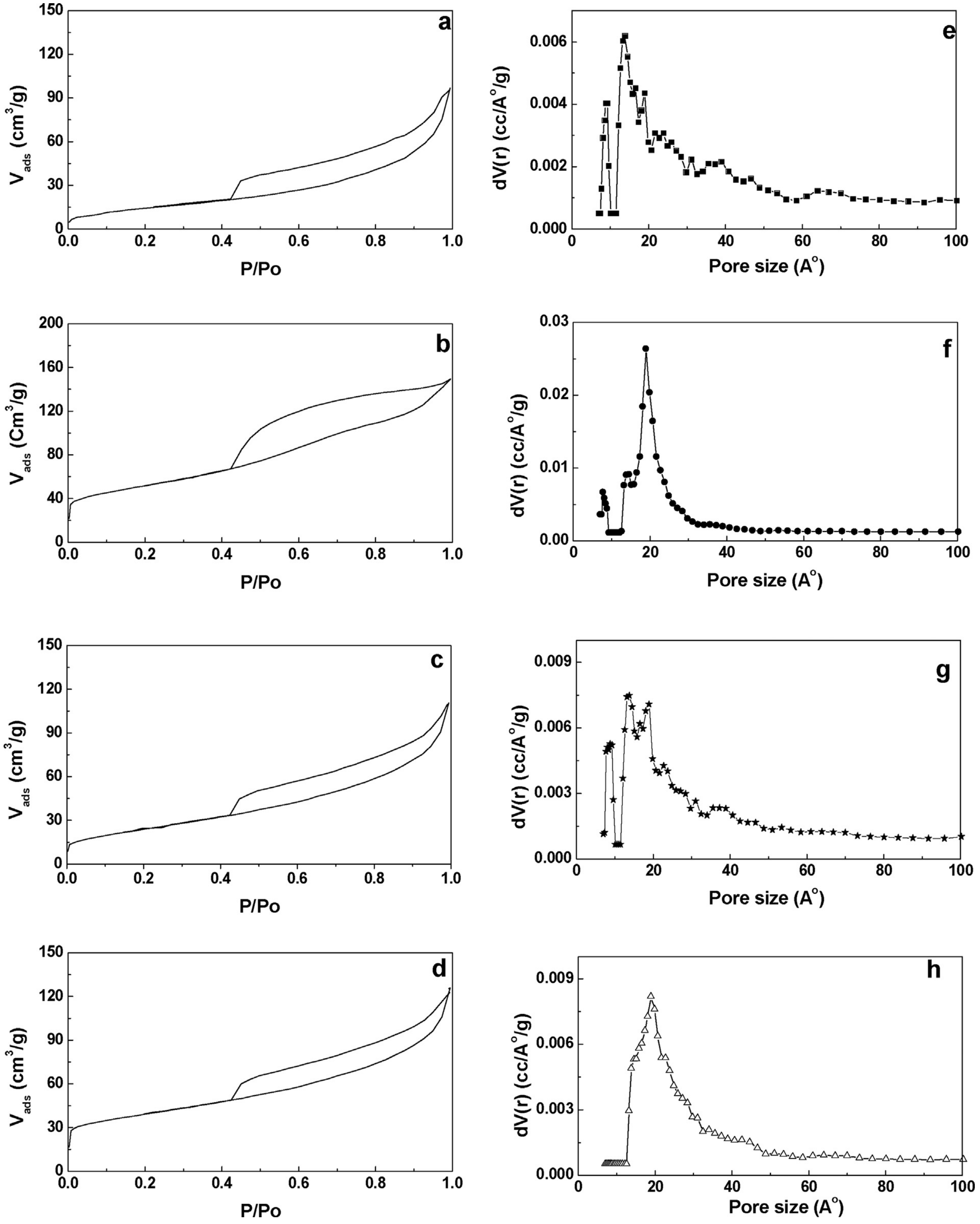

Fig. 7. N_2 sorption isotherm and pore size distribution curves of ZP (a, e), ZZP (b, f), CP_1ZZP (c, g) and CP_2ZZP (d, h) materials.

size distribution calculated using NLDFT method indicates a broad distribution profile with pore size in the range of 1.5–4 nm (Fig. 7e). Upon pillaring with Zr-polycation, the initial nitrogen adsorption is rapidly enhanced indicating an increase in the microporosity (Fig. 7b). The ZZP material show narrow pore size distribution with maxima at 1.9 nm (Fig. 7f). The adsorption features of CsxZZP materials are similar to that of ZZP material (Fig. 7c & d). The pore size distribution is broader compared to ZZP probably due to generation of secondary pore structures in presence of the CsxPWA moieties (Fig. 7g & h). It has been reported that the ion exchanged heteropoly acid display high surface area and porosity due to the reorganization of the interstitial voids in the ion exchanged sam-

Table 2
Catalytic activity of CPxZZP materials towards synthesis of spirooxindoles.

Catalyst	Catalytic activity		Conversion of α-naphthol[b]	TOF (h^{-1})
	Time (h)	Yield[a] (%)		
ZP	5	35	39	6
ZZP	5	52	55	7
CP_1ZZP	2	75	79	19
CP_2ZZP	1.5	86	88	25

[a] Refers to pure ad isolated yield.
[b] α-Naphthol conversion in the reaction mixture calculated using gas chromatography.

ples [19–24]. The surface area and pore volume of the materials are presented in Table 1. The surface area varies in the order ZP < CP_1ZZP < CP_2ZZP < ZZP.

The temperature programmed desorption profiles of CPxZZP material along with ZP and ZZP materials are presented in Fig. 8. Three ammonia desorption regions in the range of 100–200 °C, 200–350 °C and 350–450 °C could be observed for the ZP materials (Fig. 8a). These desorption peaks can be assigned to the presence of weak, medium and strong acidic sites in this material. The low temperature desorption peak is most prominent for this material indicating the presence of a large fraction of weak acidic sites. The total number of acidic sites calculated for this material is 0.23 mmol g^{-1}. The Zr-P material exhibits two broad asymmetric desorption peaks in the range of 150–350 °C and 400–600 °C (Fig. 8b). The low temperature peak can be deconvoluted into two peaks. In comparison to ZP material, the ZZP material show an incremental but significant rise in high temperature ammonia desorption indicating generation of new acidic sites of higher strength (Table 1). As observed from UV–vis study, the ZZP material contains zirconia nanoclusters with structural defects as pillars. These pillars can act as potential new acidic sites. The CPxZZP materials also exhibit two ammonia desorption peaks. However, a substantial increase in the high temperature ammonia desorption peaks are observed for these materials (Fig. 8c &d). This observation suggests that dispersion of CsxPWA species in the ZZP lattice results in generation of new medium and strong acidic sites. In order to rule out the contribution of desorbed water and/or possible surface decomposition products to this high temperature peak, blank TPD experiments were conducted without ammonia adsorption for CP_2ZZP material (Fig. S3). The TPD profile of the blank experiment does not show any appreciable desorption peak upto 600 °C. This observation indicates that the high temperature NH_3 TPD peak is due to desorbed ammonia from the strong acidic sites of the composite materials. The acidity of the CsxPWA materials has been studied earlier using TPD and calorimetry techniques [19–24]. It has been noticed that the Cs substitution increases the surface area, porosity as well as number of accessible strong acidic sties on the surface. Moreover, with increase in Cs content, the amount of strong acidic sites is increased in the CsxPWA material reaching a maximum value with $x = 2.00–2.5$ [19,21]. Hence, the improvement in the acidity observed for the composite material can be ascribed to a synergistic effect between the acidity of the host lattice and the CsxPWA material. The total number of acidic sites varies in the order CP_2ZZP > CP_1ZZP > ZZP > ZP (Table 1).

The morphological features and particle sizes of the CPxZZP materials are studied using FESEM and HRTEM techniques. The FESEM images of the CPxZZP material together with the ZP and ZZP materials are presented in Fig. 9. The α-ZrP material shows plate like particles with typical length and breadth between 180 and 250 nm and 120–160 nm, respectively (Fig. 9a). The layer to layer orientation of the α-ZrP platelets seems to be the favored orientation which is resulting into the plate like morphology. Pillaring with Zr-oligomeric cluster significantly alters the particle morphology.

Table 3
Catalytic activity of CP_2ZZP material for synthesis of structurally diverse spirooxindoles.

Sl No	1,3-diketone/Naphthol	Product	Time (h)	Yield (%)	MP (°C)
1	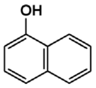	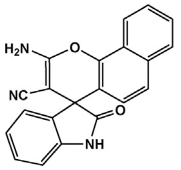	1.5	86	223–224
2	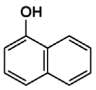	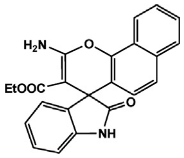	1.5	81	231
3	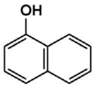	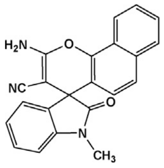	2	75	240
4	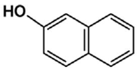	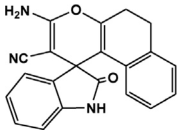	1.5	82	236
5	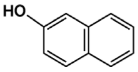	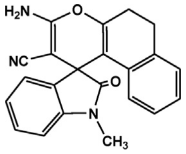	2	80	230–231
6	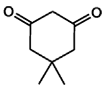	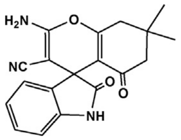	1.5	88	269–270
7	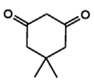	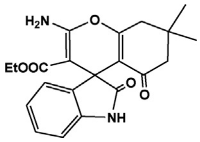	2	82	277–278
8	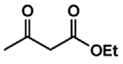	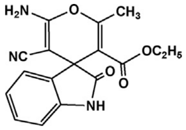	2	85	260–262
9	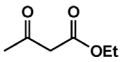	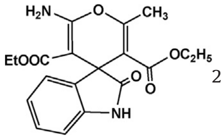	2	78	271–272
10	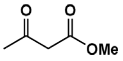	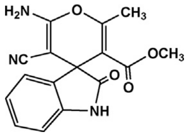	2	84	262–263
11	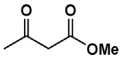	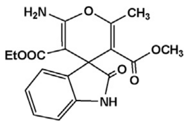	2	76	169–170

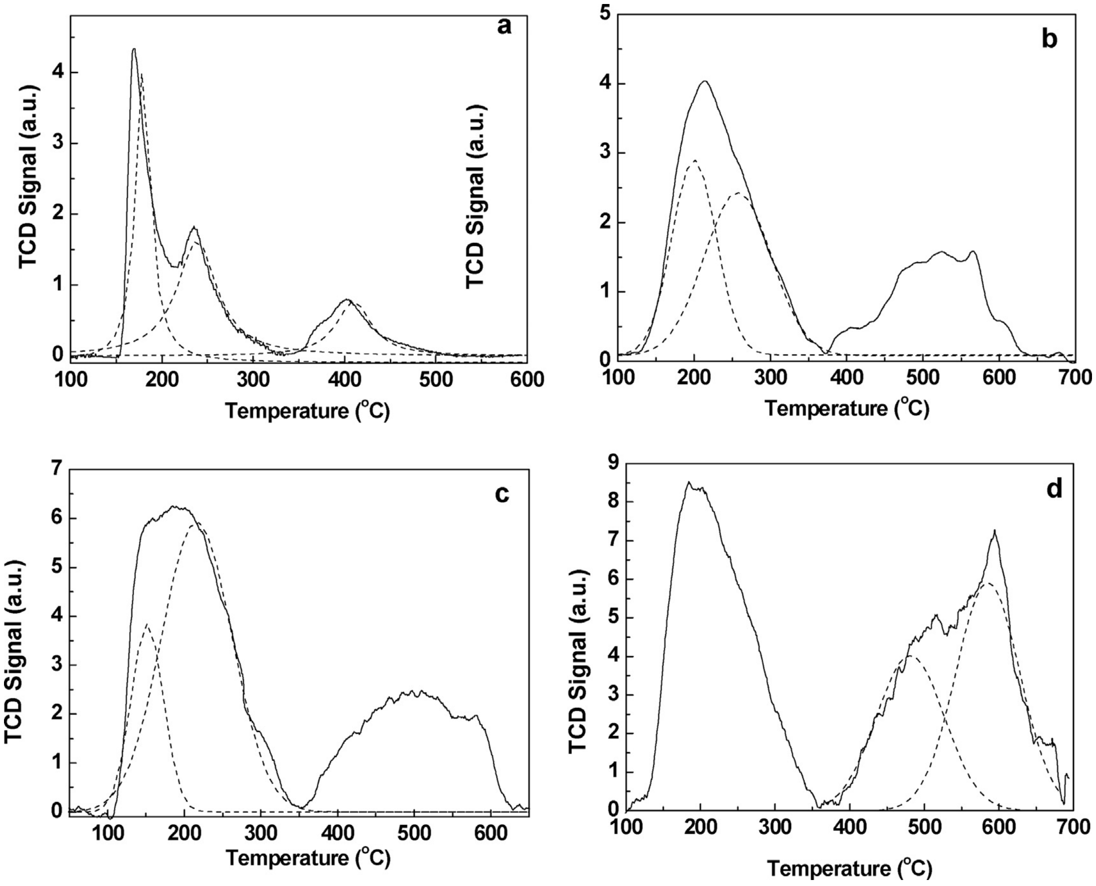

Fig. 8. TPD profiles of (a) ZP, (b) ZZP, (c) CP_1ZZP, and (d) CP_2ZZP materials.

The ZZP material contains agglomerated spherical particles with diameter in the range of 30–60 nm (Fig. 9b). The insertion of Zr-pillars imparts structural rigidity to the α-ZrP lattice. Moreover, the presence of Zr-pillars reduces the face to face interaction and facilitates edge to face and edge to edge interactions resulting in particle folding and generation of spherical particles. The spherical morphology of the particles is retained in the CPxZZP materials (Fig. 9c & d). The CP_1ZZP and CP_2ZZP materials show spherical particles with diameter in the range of 150–200 nm. The transmission electron micrographs of the CP_2ZZP material are presented in Fig. 10. The low magnification image shows a typical spherical particle with diameter 156 nm (Fig. 10a). The presence of folded α-ZrP sheets and their hierarchical organization into the spherical structure can be inferred from this TEM image. The CP_2ZZP material contains well dispersed Cs_2PWA particles with size in the range of 8–14 nm (Fig. 10a & b). The microscopic observation is further corroborating the Fourier analysis data where presence of 8–15 nm Cs_xPTA particles has been observed. The EDX pattern of the CP_2ZZP material is presented in Fig. 10c. The presence of Cs, W, Zr, P and O of required stoichiometry can be inferred from EDX study. The W/Zr atomic ratio calculated from XPS study is 0.35, which is higher than the value of 0.21 calculated from EDX measurement. This observation suggests that the CS_2PWA particles are present in a well dispersed state on the surface of ZZP matrix. The elemental mapping analysis images of the CP_2ZZP material are presented in Fig. 10d–h. Uniform distribution of the Cs and W at microscopic level can be inferred from the elemental mapping study. The EDS image clearly indicates that the Cs_2PWA nanoparticles are finely dispersed in the ZZP matrix to form the CP_2ZZP composite materials.

3.2. *Catalytic activity study for synthesis of spirooxindoles*

The catalytic activity of the CPxZZP materials has been studied for the one pot synthesis of spirooxindoles by multi-component condensation of isatin, malononitrile and naphthol/1,3-dicarbonyl compounds (Scheme 1). Initially, the condensation of isatin, malononitrile and α-naphthol is taken as a model reaction and different composite catalytic systems were studied for their catalytic activity at 60 °C using 5 ml of acetonitrile as solvent (Table 2). Pure α-ZrP material produced 35% product yield after 5 h of reaction time. The weak acidic sites on α-ZrP material are unable to expedite the spirooxindole synthesis. The product formation is marginally improved after pillaring with Zr-polycation (Table 2). The CPxZZP materials, on the other hand, show improved yield of the product in short reaction time. Among the CPxZZP materials, the CP_2ZZP material exhibits 86% yield of the product in a short time span of 1.5 h. Since the composite materials display different surface area and acidity, we calculated the turnover frequency in h^{-1} by estimating the α-naphthol conversion from the reaction mixture using GC analysis (Fig. S4). Among the different catalyst formulation studied for the reaction, the CP_2ZZP material exhibits highest turnover frequency indicating its suitability for this multicomponent reaction (Table 2). The higher catalytic activity observed for CP_2ZZP material can be correlated to the improvement in number of acidic sites which show ammonia desorption in the temperature range of 250–450 °C. In order to evaluate the role of the support (α-ZrP) on the catalytic activity, the catalytic tests are also carried out using unsupported $Cs_1H_2PW_{12}O_{40}$, $Cs_2H_1PW_{12}O_{40}$ and $H_3PW_{12}O_{40}$ materials. The results of these catalytic experiments

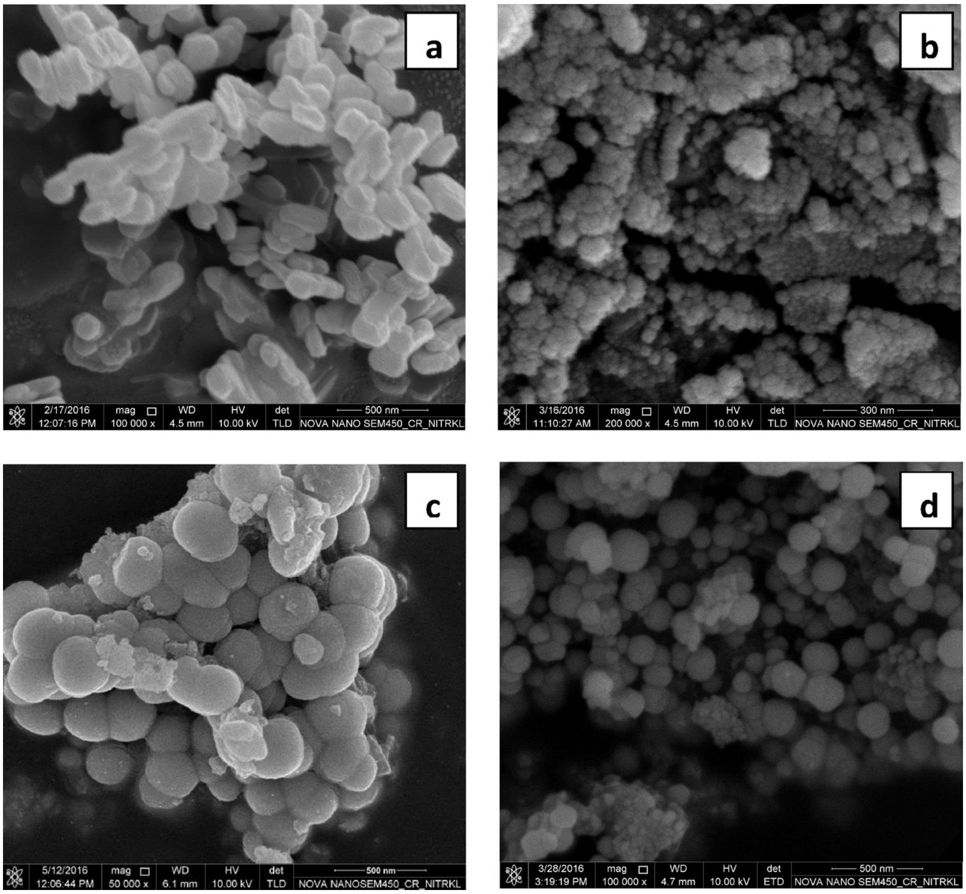

Fig. 9. FESEM images of (a) ZP, (b) ZZP, (c) CP_1ZZP, and (d) CP_2ZZP materials.

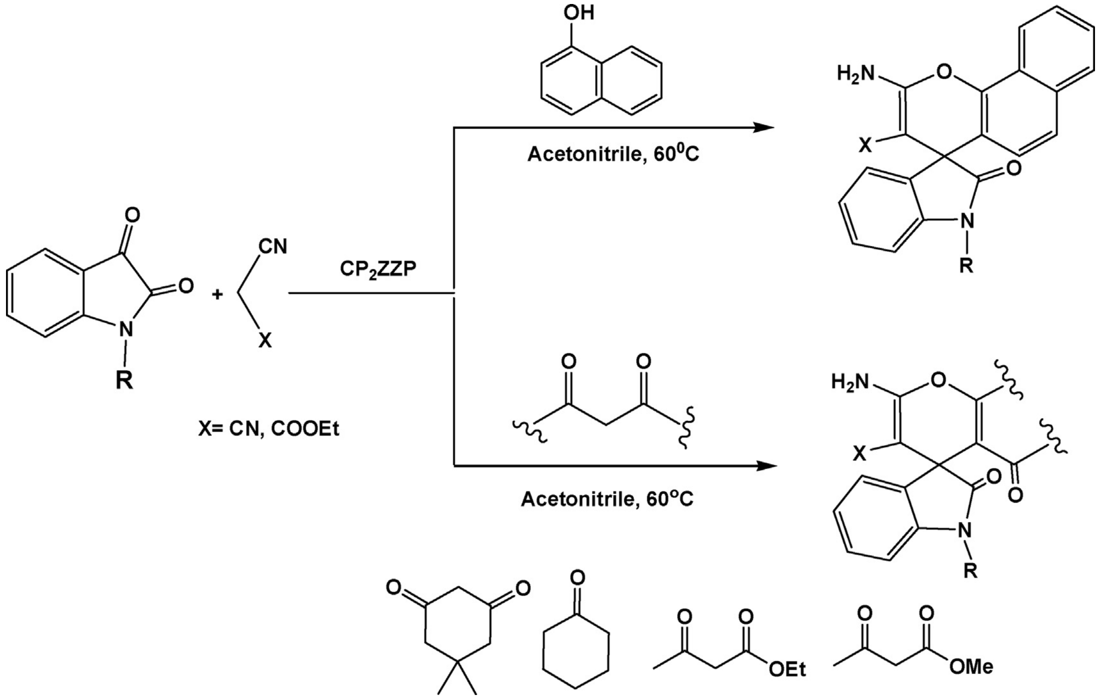

Scheme 1. CP_2ZZP catalyzed multicomponent one pot synthesis of spriooxindoles.

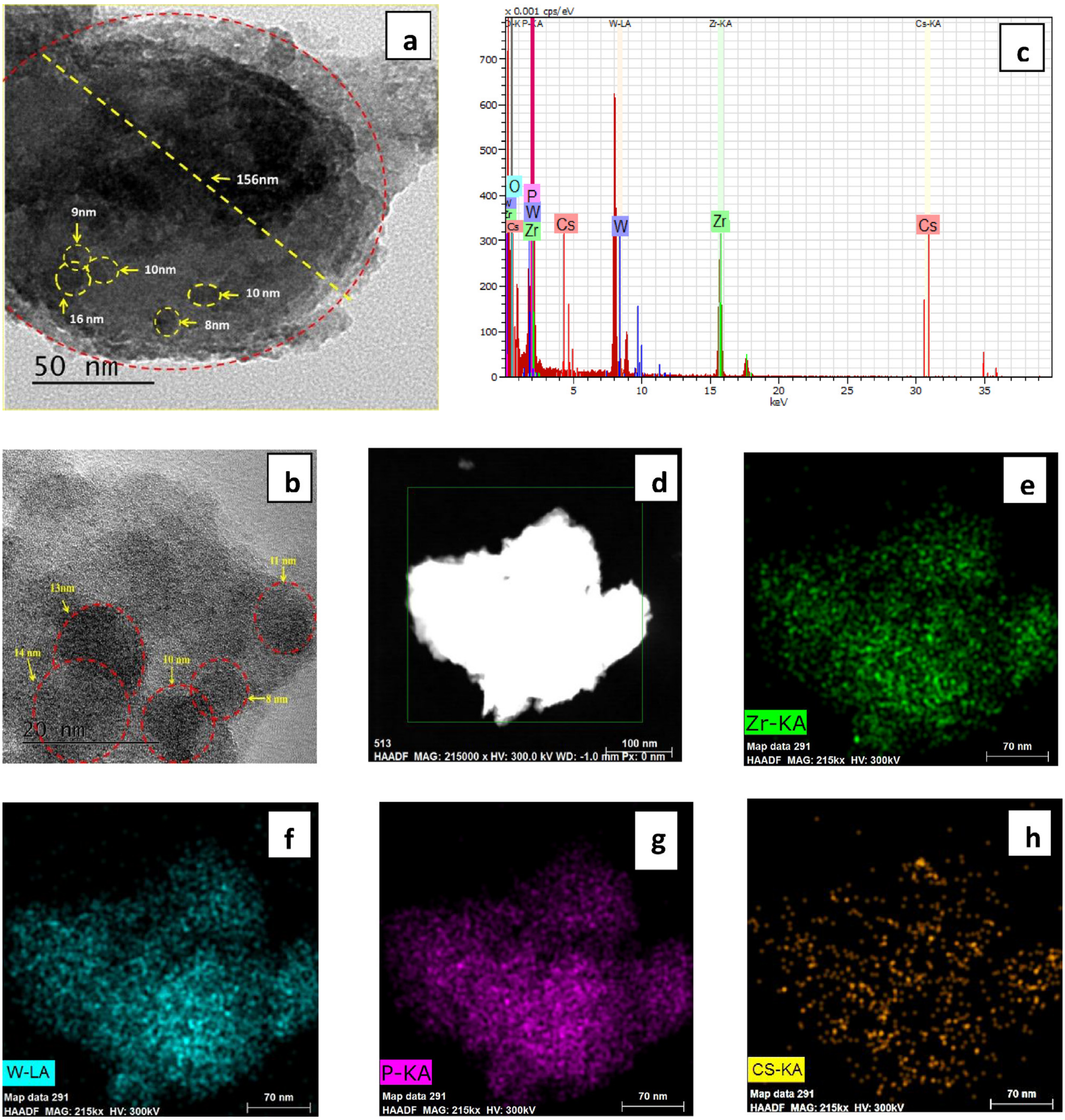

Fig. 10. HRTEM images (a, b), EDX spectra (c) and elemental mapping study (d–h) of CP_2ZZP material.

are presented in Table S1. For an identical loading amount, the CP_2ZZP material exhibits higher yield of the product compared to the pure $Cs_2H_1PW_{12}O_{40}$ material. Moreover, the $Cs_xH_{3-x}PW_{12}O_{40}$ species are more active compared to the parent $H_3PW_{12}O_{40}$ material. These observations suggest that the partial exchange of H^+ ions with Cs^+ ions is beneficial in terms of higher activity and the α-ZrP as support further enhances its catalytic activity by maximizing the dispersion of the active phase in its porous matrix. The CP_2ZZP material also exhibits higher catalytic activity compared to the $Cs_2H_1PW_{12}O_{40}$ species supported over SiO_2 and ZrO_2 (Table S1). The phosphate functionality of the support seems to be important in enhanced adsorption of the polar reactant species on the catalyst surface through van der Waal type interactions. Based on the data described in Tables Table 2 and S1, the CP_2ZZP material is selected for further catalytic study. The CP_2ZZP catalyzed reaction protocol is optimized by varying the catalyst amount, solvent and temperature (Fig. 11). For reaction involving 1 mmol of the reactants, 50 mg of the catalyst is sufficient for condensation of the three components. Further increase in catalyst quantity only marginally improves the yield (Fig. 11II). The reaction temperature is varied between 40 and 82 °C in an incremental step of 10 °C. The product yield is found to improve significantly with temperature up to 60 °C. Increase in temperature beyond 60 °C, does not have much impact on the yield of the product (Fig. 11I). To evaluate the effect of reaction media on catalytic activity, solvents with different polarity are used in the optimized protocol. In general, better yields of

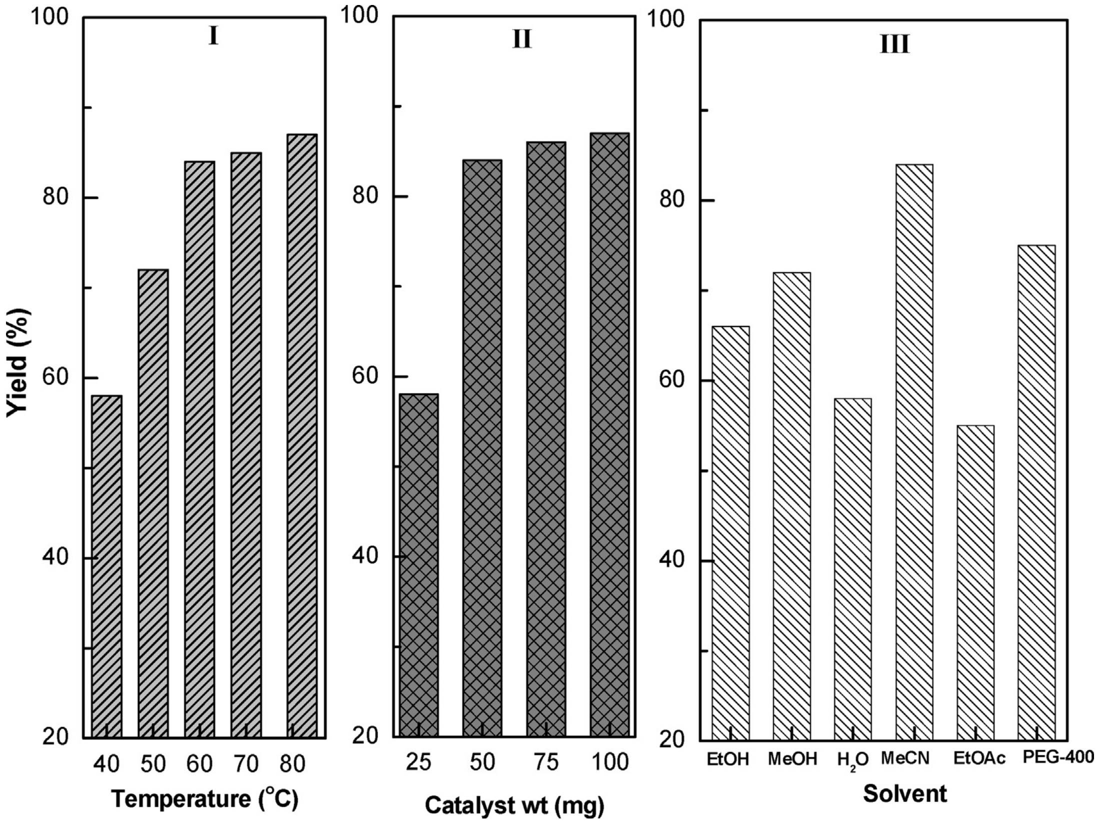

Fig. 11. Optimization of reaction parameters for the model reaction using CP_2ZZP catalyst (I) effect of temperature (acetonitrile, 50 mg catalyst) (II) Effect of catalyst amount (acetonitrile, 60 °C), and (III) effect of reaction media (50 mg catalyst, 60 °C).

the product are noticed in polar solvents. Among different solvent studied for the reaction, best yield of spirooxindole is obtained in acetonitrile (Fig. 11III). Hence, acetonitrile is used as a solvent for further study.

After optimizing the reaction conditions, we studied the scope and limitation of the optimized protocol by employing istain, malonitrile/ethyl cyanoacetate and 1-naphthol/2-naphthol in acetonitrile media at 60 °C (Table 3). Under similar experimental condition, all reactions proceed smoothly to give the corresponding spiro(tetrahydrochromene- 4,3′-indole) in high yield and purity. The CP_2ZZP catalyzed reaction protocol is extended further to three component coupling of istain, malonitrile/ethyl cyanoacetate and dicarbonyl compounds. A variety of dicarbonyl compounds including dimedone, ethyl acetoacetate and methyl acetoacetate reacted efficiently under the optimized condition to form the corresponding spirooxindole derivatives (Table 3). The recyclability of the CP_2ZZP catalyst is evaluated for three consecutive cycles. After each catalytic cycle, the catalyst particles are filtered from the reaction mixture, washed with ethanol (5 ml portions 3 times) and then heat treated at 250 °C for 2 h. The CP_2ZZP catalyst exhibits stable catalytic activity for three consecutive cycles without any significant decrease in the yield of the product (Table 3, entry 1, yields, 86.0%, 1st; 85%, 2nd; 83%, 3rd). The mechanism of spiroxyindole formation has been described in literature [34,38]. The reaction involves a cascade process, where the initial Knoevenagel condensation of isatin with malononitrile results in the formation of isatylidene malononitrile. In the second step, the ortho C-alkylation of α-naphthol takes place by reaction with the electrophilic C═C double bond of isatylidene malononitrile. The final step involves the nucleophilic addition of the phenolic OH group moiety to the cyano moiety to form the spiroxyindole. The nature of acidic sites on the composite sample has been probed using FTIR study of adsorbed pyridine for the ZZP and CP_2ZZP materials (Fig. S5). The FTIR spectra show IR bands at 1439, 1489, 1544 and 1610 cm^{-1}. The intense peak observed at 1544 cm^{-1} corresponds to pyridine adsorbed on Brønsted acidic site as pyridinium ions [52]. The peak at 1489 cm^{-1} is due to pyridine adsorbed on both Brønsted and Lewis acid sites where as the peak at 1439 and 1610 cm^{-1} can be assigned to Lewis acidic sites [52–55]. The host Zr-pillared α-ZrP lattice can contain Zr—O—P and coordinatively unsaturated zirconium ions as Lewis acidic sites [52,53]. The isatin molecule can be activated on surface low coordinated Zr^{4+} sites. The phosphate ions in the composite catalyst can enhance the adsorption of the polar reactant species through van der Waal interactions. Moreover, the α-naphthol can be activated on the catalyst surface by interaction through the π electron which can react with adsorbed isatylidene malononitrile to form the product. These features of the composite catalyst can expedite the catalytic reaction on its surface.

4. Conclusion

In this work, we have prepared a novel composite catalytic system by dispersing cesium exchanged phosphotungstic acid ($Cs_xH_{3-x}PW_{12}O_{40}$) nanoparticles in the micropores of Zr-pillared α-zirconium phosphate (ZZP) and used as catalyst for synthesis of structurally diverse spirooxinole derivatives containing chromene moieties. The pillared α-ZrP materials displayed enhanced gallery height, higher microporosity and acidity compared to the parent α-ZrP. The increased porous nature of the pillared material is successfully utilized to disperse $Cs_xH_{3-x}PW_{12}O_{40}$ nanoparticles. The structural integrity and grafting of the $Cs_xH_{3-x}PW_{12}O_{40}$ species over the ZZP material is confirmed from FTIR and UV–vis-DRS study. Study of the thermal transformation behavior of the composite materials revealed that these materials are stable upto 500 °C.

Microscopic investigation suggested the presence of well dispersed $Cs_xH_{3-x}PW_{12}O_{40}$ particles with size in the range of 8–14 nm in the composite materials. The pillaring with Zr-polycations and subsequent dispersion of the $Cs_xH_{3-x}PW_{12}O_{40}$ in the α-ZrP lattice results in generation of new medium and strong acidic sites in the composite. The composite materials exhibited excellent catalytic activity for synthesis of spirooxindoles containing fused chromene moieties by multicomponent one pot condensation of isatin, malononitrile and naphthol/1,3-dicarbonyl compounds. A variety of spirooxindole derivatives are synthesized in high yield and purity within a short time span of 1–2 h using acetonitrile as solvent. The catalytic protocol developed in this work is found to be advantageous in terms of simple experimentation, mild reaction conditions, recyclable heterogeneous catalytic system, less process time and high yield and purity of the products.

Acknowledgement

We would like to thank the Board of Research in Nuclear Sciences (BRNS), Mumbai for financial support through the grant No. 37(2)/14/23/2015/BRNS.

Appendix A. Supplementary data

Supplementary data associated with this article can be found, in the online version, at http://dx.doi.org/10.1016/j.mcat.2017.12.013.

References

[1] G. Alberti, M. Casciola, U. Costantino, R. Vivani, Adv. Mater. 8 (1996) 291–303.
[2] Z. Wang, J.M. Heising, A. Clearfield, J. Am. Chem. Soc. 125 (2003) 10375–10383.
[3] Y. Tang, Y. Ren, X. Shi, Inorg. Chem. 52 (2013) 1388–1397.
[4] F. Zhang, Y. Xie, W. Lu, X. Wang, S. Xu, X. Lei, J. Colloid Interface Sci. 349 (2010) 571–577.
[5] S. Khare, R. Chokhare, J. Mol. Catal. A: Chem. 138 (2012) 353–354.
[6] K.D. Pont, J.F. Gerard, E. Espuche, Eur. Polym. J. 48 (2012) 217–227.
[7] H. Wang, W. Liu, W. Yao, K. Zhang, J. Zhong, R. Chen, Appl. Surf. Sci. 268 (2013) 179–187.
[8] J. Xiao, J. Xu, Y. Wu, Z. Gao, Appl. Catal. A: Gen. 181 (1999) 313–322.
[9] R. Chen, J. Wang, H. Wang, W. Yao, J. Zhong, Solid State Sci. 13 (2011) 630–635.
[10] A.J. Lopez, E.R. Castellon, J.S. Gonzalez, P.B. Garcıa, E. Felici, F. Marmottini, Langmuir 16 (2000) 3317–3321.
[11] H. Mao, X. Lu, M. Li, J. Yang, B. Li, Appl. Surf. Sci. 276 (2013) 787–795.
[12] F.J.P. Reina, P.O. Pastor, E.R. Castellon, A.J. Lopez, J. Solid State Chem. 122 (1996) 231–238.
[13] K. Liu, X. Wang, S. Ding, Y. Li, W. Hua, Y. Yue, Z. Gao, J. Mol. Catal. A: Chem. 380 (2013) 84–89.
[14] N. He, Y. Yue, Z. Gao, Microporous Mesoporous Mater. 52 (2002) 1–9.
[15] J. Xu, Z. Gao, Microporous Mesoporous Mater. 24 (1998) 213–222.
[16] J.M. Robles, E.R. Castello, A.J. Lopez, J. Mol. Catal. A: Gen. 145 (1999) 169–181.
[17] R.H. Huesca, J.S. Gonzalez, P.B. Garcıa, P.M. Torres, E.R. Castellon, A.J. Lopez, Appl. Catal. B: Environ. 29 (2001) 1–11.
[18] L. Pesaresi, D.R. Brown, A.F. Lee, J.M. Montero, H. Williams, K. Wilson, Appl. Catal. A: Gen. 360 (2009) 50–58.
[19] K. Narasimharao, D.R. Brown, A.F. Lee, A.D. Newman, P.F. Siril, S.J. Tavener, K. Wilson, J. Catal. 248 (2007) 226–234.
[20] N.R. Shiju, H.M. Williams, D.R. Brown, Appl. Catal. B: Environ. 90 (2009) 451–457.
[21] H.J. Eom, D.W. Lee, S. Kim, S.H. Chung, Y.G. Hur, K.Y. Lee, Fuel 126 (2014) 263–270.
[22] K. Srilatha, R. Sree, B.L.A.P. Devi, P.S. Sai Prasad, R.B.N. Prasad, N. Lingaiah, Bioresour. Technol. 116 (2012) 53–57.
[23] C.R. Kumar, S. Gatla, O. Mathon, S. Pascarelli, N. Lingaiah, Appl. Catal. A: Gen. 502 (2015) 297–304.
[24] A. Popa, V. Sasc, I.H. Antunovic, Microporous Mesoporous Mater. 156 (2012) 127–137.
[25] K.T.V. Rao, P.S.N. Rao, P.S. Sai Prasad, N. Lingaiah, Catal. Commun. 10 (2009) 1394–1397.
[26] M. Srinivas, G. Raveendra, G. Parameswaram, P.S. Sai Prasad, N. Lingaiah, J. Mol. Catal. A: Chem. 413 (2016) 7–14.
[27] A. Srikanth, B. Viswanadham, V.P. Kumar, N. Rao Anipindi, K.V.R. Chary, Appl. Petrochem. Res. 6 (2016) 145–153.
[28] R.J. Sundberg, The Chemistry of Indoles, Academic Press, New York, 1996.
[29] T.R. Garbe, M. Kobayashi, N. Shimizu, N. Takesue, M. Ozawa, H. Yukawa, J. Nat. Prod. 63 (2000) 596–598.
[30] R.M. Williams, R.J. Cox, Acc. Chem. Res. 36 (2003) 127–139.
[31] N. Yu, J.M. Aramini, M.W. Germann, Z. Huang, Tetrahedron Lett. 41 (2000) 6993–6996.
[32] L. Bonsignore, G. Loy, D. Secci, A. Calignano, Eur. J. Med. Chem. 28 (1993) 517–520.
[33] A. Kamal, K.S. Babu, M.V.P.S.V. Vardhan, S.M.A. Hussaini, R. Mahesh, S.P. Shaik, A. Alarifi, Bioorg. Med. Chem. Lett. 25 (2015) 2199–2202.
[34] G. Shanthi, G. Subbulakshmi, P.T. Perumal, Tetrahedron 63 (2007) 2057–2063.
[35] L.M. Wang, N. Jiao, J. Qiu, J.J. Yu, J.Q. Liu, F.L. Guo, Y. Liu, Tetrahedron 66 (2010) 339–343.
[36] M. Esmaeilpour, J. Javidi, M. Divar, J. Magn. Magn. Mater. 423 (2017) 232–240.
[37] G.M. Ziarani, A. Badiei, S. Mousavi, N. Lashgari, A. Shahbazi, Chin. J. Catal. 33 (2012) 1832–1839.
[38] A. Dandia, V. Parewa, A.K. Jain, K.S. Rathore, Green Chem. 13 (2011) 2135–2145.
[39] B. Karmakar, A. Nayak, J. Banerji, Tetrahedron Lett. 53 (2012) 5004–5007.
[40] F.A. Tameh, J.S. Ghomi, M.M. Hashemi, H.S. Alavi, RSC Adv. 6 (2016) 74802–74811.
[41] P. Kar, A. Nayak, Y.P. Bhoi, B.G. Mishra, Microporous Mesoporous Mater. 223 (2016) 176–186.
[42] T. Okuhara, T. Nakato, Catalysis by porous heteropoly compounds, Catal. Surv. Asia 2 (1998) 31–44.
[43] B.E. Warren, B.L. Averbach, J. Appl. Phys. 21 (1950) 595–599.
[44] S. Samantaray, B.G. Mishra, D.K. Pradhan, G. Hota, Ceram. Int. 37 (2011) 3101–3108.
[45] S. Samantaray, B.G. Mishra, J. Mol. Catal. A: Chem. 339 (2011) 92–98.
[46] G.R. Rao, T. Rajkumar, Catal. Lett. 120 (2008) 261–273.
[47] J.L. Colon, D.S. Thakur, C.Y. Yang, A. Clearfield, C.R. Martin, J. Catal. 124 (1990) 148–159.
[48] S. Pradhan, V. Sahu, B.G. Mishra, J. Mol. Catal. A: Chem. 425 (2016) 297–309.
[49] P.A. Jalil, M. Faiz, N. Tabet, N.M. Hamdan, Z. Hussain, J. Catal. 217 (2003) 292–297.
[50] R. Weingarten, Y.T. Kim, G.A. Tompsett, A. Fernandez, K.S. Han, E.W. Hagaman, W.C. Conner Jr., J.A. Dumesic, G.W. Huber, J. Catal. 304 (2013) 123–134.
[51] S.J. Gregg, K.S.W. Sing, Adsorption, Surface Area and Porosity, Academic Press, London, 1982.
[52] F. Li, L.J. France, Z. Cai, Y. Li, S. Liu, H. Lou, J. Long, X. Li, Appl. Catal. B: Environ. 214 (2017) 67–77.
[53] G. Busca, V. Lorenzelli, P. Galli, A. Ginestra, P. Patrono, J. Chem. Soc. Faraday Trans. 83 (1987) 853–864.
[54] D. Cao, B. Yu, S. Zhang, L. Cui, J. Zhang, W. Cai, Appl. Catal. A: Gen. 528 (2016) 59–66.
[55] A.E.R.S. Khader, S.A. Ahmed, H.M. Altass, React. Kinet. Mech. Catal. 117 (2016) 745–759.